



GPR Measurements Inversion in Case of Spatially Varying Antenna Polarization

Jianping Wang, Pascal Aubry, and Alexander Yarovoy*
Delft University of Technology, Delft, The Netherlands

Abstract

In this paper, Ground Penetrating Radar (GPR) imaging with arbitrarily oriented antennas within the data acquisition aperture is studied. The variations of antenna orientations change both the polarization of the radiated electromagnetic fields and spatial radiation patterns, which are assumed to be constant in traditional imaging algorithms. To overcome these effects, a linear inversion scheme is proposed by considering the exact radiation patterns of antennas. In terms of implementation, spatially varied radiation patterns are needed for arbitrarily orientated antennas. To efficiently acquire the radiation patterns, we suggest an interpolation-based method to compute the accurate Green's functions. Moreover, thanks to the frequency domain modeling, the proposed linear inversion approach also facilitates the signal fusion of multi-band GPR measurements for improved imaging, which is necessary for some practical applications. Finally, the imaging performance of the linear inversion approach is demonstrated through a numerical experiment.

1 Introduction

Nowadays, GPR has been broadly used for land mine detection, road pavement inspection, underground facilities survey, archaeological investigation, etc. [1]. This list is still expanding. One of the recent GPR applications is for ground prediction in the tunnel boring machine (TBM) which is a very important piece of equipment for excavating tunnels [2,3]. The TBM replaces the traditional "hand mining" manner and avoids the human exposure to the harsh environment. However, some potential risks still exist during the excavation of TBM.

To avoid or reduce these risks, a GPR system mounted on the cutter head of the TBM is used to monitor the ground in front of the TBM during its advancement. The GPR measurements are acquired during the rotation of the cutter head. Therefore, a circular antenna aperture is synthesized. Due to the rotated signal acquisition scheme, the antenna orientation varies spatially over the data acquisition aperture. Thus the radiation patterns of antennas are rotated and the polarization of radiated electromagnetic waves changes as well. This is distinct from the traditional GPR systems where the antenna orientations keep constant over

the aperture as assumed by traditional GPR imaging algorithms. Thus the invalidity of this assumption would lead to degraded quality of the GPR images focused with the traditional imaging algorithms.

To overcome these effects, we formulate the imaging process as a linear inverse problem by accounting for the spatially varied radiation patterns of the antennas. Although the effects of radiation patterns of GPR antennas have been studied and also taken into account to improve GPR imaging, these open literature mainly focus on the traditional GPR systems where the measurements are acquired with orientation-aligned antennas over the aperture [4–6]. In [4], Moran *et al.* studied the effects of the GPR antenna radiation patterns on the 3-D Kirchhoff migration imaging. In [6], the GPR signal responses for different transmit and receive antenna configurations, i.e., broadside and end-fire were investigated. Moreover, the exact radiation patterns of the GPR antennas were integrated into the matrix-based multicomponent imaging operation in [5] and a Fast Fourier transform (FFT) based method was suggested to efficiently compute the accurate Green's functions. However, the matrix based multicomponent imaging algorithm also assumes that the orientations of GPR antennas are constant within the aperture. Regarding the accurate Green's function computation, the varied orientations of antennas induce the spatial rotation of the radiation patterns. So the radiation patterns of rotated antennas within the aperture are not only linear translated but also rotated in a fixed rectangular coordinate system. To address this problem, we propose an interpolation based method to compute the accurate Green's functions for rotated antennas.

The rest of the paper is organized as follows. In section 2, GPR imaging with the polarization-varied measurements is modeled and formulated as a linear inverse problem. Then an interpolation based method for computing accurate Green's functions for rotated antennas is discussed in section 3. In section 4, the performance of the proposed approach for GPR imaging is demonstrated via a numerical experiment. Finally, conclusions are drawn in section 5.

2 Formulation

Fig. 1 illustrates the geometry of the forward-looking GPR imaging with rotated antennas. The transmit and receive

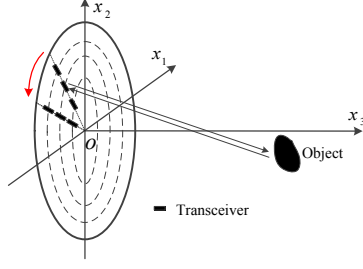


Figure 1. Illustration of forward-looking microwave imaging with rotated antennas.

antennas are placed along a radius of a circular aperture on the x_1x_2 plane and oriented parallel to the radius. The x_3 -axis points to the scene of interest and forms a right-handed coordinate system. With the rotation of the transmit and receive antenna arrays, the antennas illuminate the scene of interest and the scattered signals are acquired over the space. Consequently, an equivalent circular antenna array is synthesized. Based on the Born approximation, the scattered electromagnetic signals for a pair of transmit and receive antennas can be represented as [7]

$$\begin{aligned} E_{\alpha\beta}^s(\mathbf{x}^R, \mathbf{x}^T, \omega) &= \int_{V(\mathbf{x}^c)} D_{\alpha\beta}(\mathbf{x}^R, \mathbf{x}^T | \mathbf{x}^c, \omega) \otimes \chi(\mathbf{x}^c) J_{\beta}(\mathbf{x}^T, \omega) dV \\ &= S(\omega) \int_{V(\mathbf{x}^c)} D_{\alpha\beta}(\mathbf{x}^R, \mathbf{x}^T | \mathbf{x}^c, \omega) b_{\beta}(\mathbf{x}^T, \omega) \chi(\mathbf{x}^c) dV \end{aligned} \quad (1)$$

where \otimes denotes the spatial convolution, $D_{\alpha\beta}$ is the wavefield extrapolator from a point source J_{β} at \mathbf{x}^T to a scatterer at \mathbf{x}^c and then to a receiver at \mathbf{x}^R , where the subscripts α and β represent the polarizations of transmit and receive antennas. The contrast function $\chi(\mathbf{x}^c)$ is defined as the difference of the background physical property $\hat{\eta}$ and scatterer's physical property η , i.e., $\chi(\mathbf{x}^c) = \hat{\eta} - \eta$. Here η is defined as $\eta = \sigma + j\omega\epsilon$, where σ is the conductivity and ϵ is the permittivity. Moreover, in the last line of (1), the expression $J_{\beta}(\mathbf{x}^T, \omega) = S(\omega) \mathbf{b}_{\beta}(\mathbf{x}^T, \omega) J_{\beta}(\mathbf{x}^T, \omega)$ has been used for a point source, where $S(\omega)$ is the wavelet and $\mathbf{b}_{\beta}(\mathbf{x}^T, \omega)$ denotes the polarization vector. In space, the wavefield extrapolator $D_{\alpha\beta}$ is explicitly written as an inner product of the Green's functions of transmit and receive antennas

$$D_{\alpha\beta} = \sum_{l=1}^3 G_{\alpha l} G_{l\beta} \quad (2)$$

where $l \in \{1, 2, 3\}$ represents the electric field orthogonal directions. $G_{\alpha l}$ and $G_{l\beta}$ are the Green's functions in the l direction for α -pol receive and β -pol transmit antennas, respectively. In the discrete form, (1) can be written as

$$E_{\alpha\beta}^s(\mathbf{x}^R, \mathbf{x}^T, \omega) = S(\omega) \cdot \Delta V \cdot \sum_{k=1}^{N_p} D_{\alpha\beta}(\mathbf{x}^T, \mathbf{x}^R | \mathbf{x}_k^c, \omega) \chi(\mathbf{x}_k^c) \quad (3)$$

where N_p is the number of partition cells of the imaging scene and ΔV is the volume of each partition cell. $S(\omega)$ is the spectrum of the wavelet. Considering all the transmit and receive antenna pairs and all the frequencies of the signals, scattered signals can be represented in a matrix form

$$\mathbf{E}^s = \mathbf{D}_{N_{tr} \times N_p} \cdot \chi(\mathbf{X}^c) \quad (4)$$

where N_{tr} is the number of transmit-receive antenna pairs. In (4), the constant $S(\omega) \cdot \Delta V$ has been normalized with respect to the spectrum of each frequency. \mathbf{D} denotes the matrix of the forward wavefield extrapolator with entries obtained by (2). $\chi(\mathbf{X}^c) = [\chi(\mathbf{x}_1^c) \ \chi(\mathbf{x}_2^c) \ \cdots \ \chi(\mathbf{x}_{N_p}^c)]^T$ is a vector of the contrast functions of the pixels, where superscript \top refers to the matrix transpose operation and $\mathbf{x}_1^c, \mathbf{x}_2^c, \cdots, \mathbf{x}_{N_p}^c$ are the positions related to each pixel in the imaging scene. To reconstruct the image of scatters, a least squares estimation of the contrast functions of the scatters can be obtained

$$\chi(\mathbf{X}^c) = \mathbf{D}^\dagger \cdot \mathbf{E}^s \quad (5)$$

where $\mathbf{D}^\dagger = (\mathbf{D}^H \mathbf{D})^{-1} \mathbf{D}^H$, and the superscript H and $(\cdot)^{-1}$ are the Hermitian transpose and the inverse operation of a matrix. To circumvent the inverse operation of a large matrix $\mathbf{D}^H \mathbf{D}$, some iterative approaches can be used to solve (5). In this paper, we used the BiConjugate Gradient Stabilized method (BiCGStab).

Moreover, thanks to the frequency-domain formulation for the GPR imaging as a linear inverse problem, multiband signal fusion can be conveniently implemented, which is attractive for the case where wideband GPR measurements are acquired via multiple relatively narrow-band antennas. By stacking the multiband GPR measurements together with the corresponding wave field extrapolator vectors in the form of (4), the multiband information can be integrated into a focused image through linear inversion.

3 Green's Functions Computation for Rotated Antennas

To construct the wave field extrapolator matrix in (4), accurate Green's functions of rotated antennas are needed. For a dipole antenna placed on the surface of homogeneous ground, the exact Green's functions can be written as [5]

$$\begin{pmatrix} G_{11} & G_{12} \\ G_{21} & G_{22} \\ G_{31} & G_{32} \end{pmatrix} = -\zeta \begin{pmatrix} k_1^2 V + U & k_1 k_2 V \\ k_1 k_2 V & k_2^2 V + U \\ -jk_1 \Gamma_0 V & -jk_2 \Gamma_0 V \end{pmatrix} \quad (6)$$

where

$$U = \frac{\exp(-\Gamma_1 x_3)}{\Gamma_0 + \Gamma_1}, \quad V = \frac{\exp(-\Gamma_1 x_3)}{\gamma_1^2 \Gamma_0 + \gamma_0^2 \Gamma_1} \quad (7)$$

and $\Gamma_i = \sqrt{\gamma_i^2 + k_1^2 + k_2^2}$. $\gamma_i^2 = \eta_i \zeta$ represents complex propagation constants for air ($i = 0$) and the subsurface ($i = 1$); $\eta_i = \sigma_i + j\omega\epsilon_i$ is the electric material parameter

for the conductivity σ_i and the permittivity ϵ_i ; $\zeta = j\omega\mu_0$ is the magnetic material parameter with permeability μ_0 ; k_1 and k_2 are the wavenumbers on the aperture plane; $\omega = 2\pi f$ is the angular frequency with respect to the frequency f . Taking inverse Fourier transform (IFT) of the Green's functions in (6) with respect to k_1 and k_2 , their counterparts in the space-frequency (i.e., x - f) domain are obtained $\begin{pmatrix} g_{11}(x_1, x_2, f) & g_{21}(x_1, x_2, f) & g_{31}(x_1, x_2, f) \\ g_{12}(x_1, x_2, f) & g_{22}(x_1, x_2, f) & g_{32}(x_1, x_2, f) \end{pmatrix}^\top$.

As in (6) it assumes that the antenna at $(0, 0, 0)$ is placed along the x_1 or x_2 axis, so the exact Green's functions for antennas shifted over rectangular grids in $x_1 \times x_2$ coordinate system can be obtained via the linear translation in space. However, for rotated antenna arrays, the antennas are not only translated but also rotated within the aperture, which leads to the translation and rotation of their radiation patterns in space. Anyhow, the radiation pattern of a rotated antenna in a coordinate system defined by its axis and the orthogonal direction is still can be efficiently computed by taking IFT of (6).

To obtain the exact Green's function for rotated antennas in x_1 - x_2 - x_3 coordinate system, both the translation and rotation effects should be taken into account. At first, we define the imaging grid in space at a certain depth as

$$I = \left\{ (x_{1p}, x_{2q}) \left| \begin{array}{l} x_{1p} = p\Delta x_1, p = 0, 1, \dots, N_{x_1} - 1; \\ x_{2q} = q\Delta x_2, q = 0, 1, \dots, N_{x_2} - 1 \end{array} \right. \right\} \quad (8)$$

where Δx_1 , Δx_2 are the grid intervals in the x_1 and x_2 directions and N_{x_1} , N_{x_2} are the associated numbers of sample points. For a dipole antenna at $(x_1^a, x_2^a, 0)$ rotated by an angle of θ with respect to the x_1 -axis, as indicated above, its Green's functions in the wavenumber-frequency domain can be directly obtained by (6) in terms of a "local" coordinate system defined by the antenna axis (denoted as x_θ) and its normal direction (x_{θ_\perp}). More precisely, the "local" coordinate system is defined as x_θ - x_{θ_\perp} - x_3 with the origin at $(x_1^a, x_2^a, 0)$, and the Fourier counterparts of x_θ and x_{θ_\perp} are denoted as k_θ and k_{θ_\perp} . Then in the "local" k_θ - k_{θ_\perp} - f domain, the Green's functions $G_{\theta\theta_\perp}$ can be directly computed via (6) on a grid Φ defined as

$$\Phi = \left\{ (k_\theta^{(m)}, k_{\theta_\perp}^{(n)}) \left| \begin{array}{l} k_\theta^{(m)} = m\Delta k_\theta; m = 0, 1, \dots, L_{k_\theta} - 1 \\ k_{\theta_\perp}^{(n)} = n\Delta k_{\theta_\perp}; n = 0, 1, \dots, L_{k_{\theta_\perp}} - 1 \end{array} \right. \right\} \quad (9)$$

where Δk_θ and Δk_{θ_\perp} are the sampling intervals determined by the field of view of the imaging scene according to the Nyquist criterion. In practice, it is necessary to take 4~16 times more samples in the k - f domain to get sufficiently accurate radiation patterns of antennas, especially for the near field.

To get the Green's functions of a rotated antenna on the imaging grid I , two steps are needed. At first, Green's functions $g_{\theta\theta_\perp}^a(x_\theta, x_{\theta_\perp}, \omega)$ in the x_θ - x_{θ_\perp} - f domain are obtained by taking IFFT of $G_{\theta\theta_\perp}(k_\theta, k_{\theta_\perp}, f)$ with respect to k_θ and

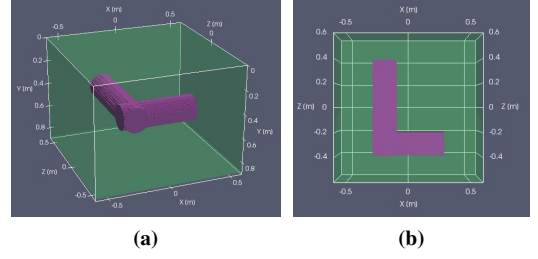


Figure 2. GPR simulation setup. (a) 3-D Geometrical configuration, and (b) its top view.

k_{θ_\perp} . Then a mapping of Green's functions from x_θ - x_{θ_\perp} to grid I is required, which is written as

$$g^a(x_1, x_2, f; x_1^a, x_2^a, \theta) = g_{\theta\theta_\perp}^a(\tilde{x}_\theta, \tilde{x}_{\theta_\perp}) \quad (10)$$

where

$$\begin{aligned} \tilde{x}_\theta &= (x_1 - x_1^a) \cos \theta + (x_2 - x_2^a) \sin \theta \\ \tilde{x}_{\theta_\perp} &= -(x_1 - x_1^a) \sin \theta + (x_2 - x_2^a) \cos \theta \end{aligned}$$

The mapping in (10) can be implemented by many interpolation methods, such as nearest, cubic, spline. In this paper, spline interpolation was used by accounting for both accuracy and efficiency.

4 Simulations

A three-dimensional (3-D) GPR imaging experiment was performed to demonstrate the proposed linear inversion approach. The simulation setup is shown in Fig. 2. Two dielectric cylinders of radius 10 cm were used to represent the underground cavities. They were buried at the depth of 0.4 m below the ground surface, and their dielectric permittivity and conductivity are 5.0 and 0.05 S/m, respectively. The relative permittivity and conductivity of the background soil are 9.0 and 0.01 S/m. The GPR transmit and receive antenna pairs were deployed on the ground surface (xoz plane). GPR measurements were acquired over eight circles centered at the origin with the radius ranging from 0.15 to 0.5m with steps of 5cm. Over each circle, measurements were taken every 2.4° in azimuth. At each sampling position, the transmit and receive antennas were separated in azimuth with an interval of 4 cm. The Ricker wavelet of 900 MHz was used as the exciting signal. The synthetic electromagnetic data were generated with the Finite-Difference Time-Domain (FDTD) software gprMax [8].

Taking the Fourier transform of the Ricker wavelet with respect to time, the 3-dB effective signal bandwidth was determined as 550~1550 MHz. Taking advantage of the frequency-domain measurements with steps of 12.7 MHz within the effective bandwidth and the computed radiation patterns of rotated antennas, a linear system as (4) can be established. The reconstructed images via linear inversion are shown in Fig. 3 (e) and (f). Meanwhile, to investigate the signal fusion potential via linear inversion, the effective bandwidth was split into two subbands: 550~950

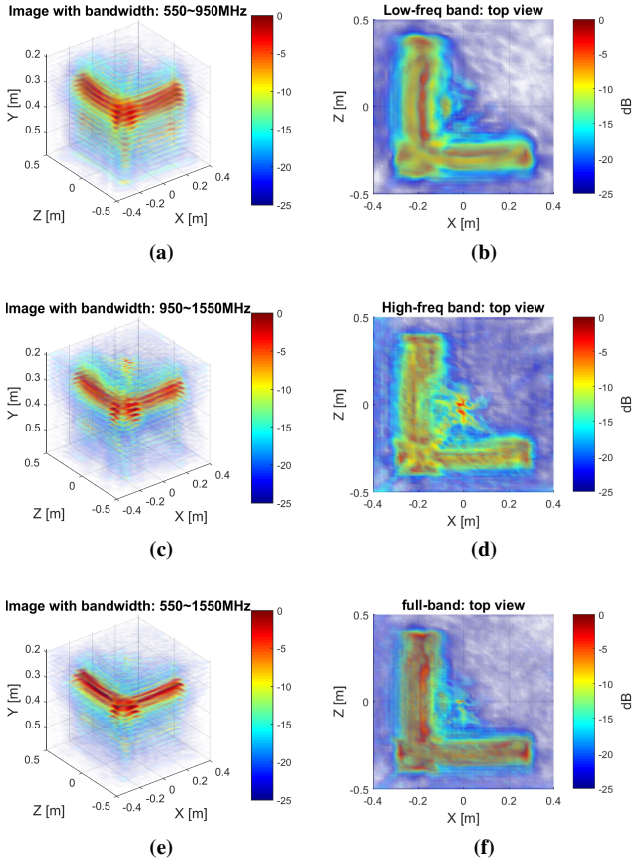


Figure 3. Reconstructed images with the linear inversion approach. (a), (c) and (e) show the 3-D images obtained with low-frequency (550~950 MHz), high-frequency (950~1550 MHz) and full-band (550~1550 MHz) signals. (b), (d), and (f) are their top-view images.

MHz and 950~1550 MHz. The estimated images with the two subband signals are presented in Fig. 3 (a)-(d). Comparing the 3-D images obtained with different bandwidths (Fig. 3 (a), (c) and (e)), one can see that the image with full-band signals achieves the best resolution, especially in the down-range direction, and the profile of the target is neatly reconstructed. Moreover, the artifacts are significantly suppressed in the full-band images (see Fig. 3 (f)). Here we have to mention that for the multiband signals acquired with separate GPR systems some pre-processing are needed to compensate the weighting effects of the signal spectra. If frequency gaps exist among the multiband signals, signal interpolation/extrapolation via model-based estimation methods could further improve the resolution of the estimated image.

5 Conclusion

In this paper, the GPR imaging with polarization-varied measurements was studied. To overcome the effects of the variance of antenna orientations within the aperture, the GPR imaging was formulated as a linear inverse problem by considering the exact radiation patterns. An interpolation-

based method was suggested to efficiently compute the spatially varied radiation patterns of rotated antennas. The effectiveness of the proposed inversion scheme has been demonstrated through a numerical imaging experiment. Moreover, the imaging results also illustrate the feasibility of the linear inversion scheme to fuse multiband GPR measurements.

6 Acknowledgements

This work is partially supported by NeTTUN project funded by European Commission within the FP-7 framework programme under Grant 280712.

References

- [1] D. Daniels, *Ground Penetrating Radar, 2nd Edition*. Institution of Engineering and Technology, 2004.
- [2] T. Sato, K. Takeda, T. Nagamatsu, T. Wakayama, I. Kimura, and T. Shinbo, "Automatic signal processing of front monitor radar for tunneling machines," *Geoscience and Remote Sensing, IEEE Transactions on*, vol. 35, no. 2, pp. 354–359, 1997.
- [3] J. Wang, H. Cetinkaya, A. Yarovoy, I. I. Vermesan, and S. Reynaud, "Investigation of forward-looking synthetic circular array for subsurface imaging in tunnel boring machine application," in *Advanced Ground Penetrating Radar (IWAGPR), 2015 8th International Workshop on*, pp. 1–4.
- [4] M. L. Moran, S. A. Arcone, and R. J. Greenfield, "GPR radiation pattern effects on 3D kirchhoff array imaging," pp. 208–212, 2000.
- [5] R. Streich and J. van der Kruk, "Accurate imaging of multicomponent GPR data based on exact radiation patterns," *Geoscience and Remote Sensing, IEEE Transactions on*, vol. 45, no. 1, pp. 93–103, 2007.
- [6] D. C. Nobes and A. P. Annan, "'broadside" versus "end-fire" radar response: some simple illustrative examples," pp. 696–701, 2000.
- [7] J. Kruk, C. Wapenaar, J. Fokkema, and P. van den Berg, "Three-dimensional imaging of multicomponent ground penetrating radar data," *GEOPHYSICS*, vol. 68, no. 4, pp. 1241–1254, 2003.
- [8] C. Warren, A. Giannopoulos, and I. Giannakis, "gprmax: Open source software to simulate electromagnetic wave propagation for ground penetrating radar," *Computer Physics Communications*, vol. 209, pp. 163–170, 2016.